Complex shallow mantle beneath the Dharwar Craton inferred from Rayleigh wave inversion

Kajaljyoti Borah,[1] S. S. Rai,[1] Keith Priestley[2] and V. K. Gaur[3,4]

[1]*National Geophysical Research Institute, Uppal Road, Hyderabad* 500 007, *India. E-mail:* kajalborah1979@gmail.com
[2]*Bullard Laboratories, Cambridge University, Cambridge CB3 0EZ, United Kingdom*
[3]*Indian Institute of Astrophysics, Bangalore* 560034, *India*
[4]*CSIR Fourth Paradigm Institute, Bangalore* 560034, *India*

SUMMARY

The 3-D shear velocity structure beneath South India's Dharwar Craton determined from fundamental mode Rayleigh waves phase velocities reveals the existence of anomalously high velocity materials in the depth range of 50–100 km. Tomographic analysis of seismograms recorded on a network of 35 broad-band seismographs shows the uppermost mantle shear wave speeds to be as high as 4.9 km s^{-1} in the northwestern Dharwar Craton, decreasing both towards the south and the east. Below ∼100 km, the shear wave speed beneath the Dharwar Craton is close to the global average shear wave speed at these depths. Limitations of usable Rayleigh phase periods, however, have restricted the analysis to depths of 120 km, precluding the delineation of the lithosphere–asthenosphere boundary in this region. However, pressure–temperature analysis of xenoliths in the region suggests a lithospheric thickness of at least ∼185 km during the mid-Proterozoic period. The investigations were motivated by a search for seismic indicators in the shallow mantle beneath the distinctly different parts of the Dharwar Craton otherwise distinguished by their lithologies, ages and crustal structure. Since the ages of cratonic crust and of the associated mantle lithosphere around the globe have been found to be broadly similar and their compositions bimodal in time, any distinguishing features of the various parts of the Dharwar shallow mantle could thus shed light on the craton formation process responsible for stabilizing the craton during the Meso- and Neo-Archean.

Key words: Composition of the mantle; Surface waves and free oscillations; Seismic tomography; Cratons; Asia.

1 INTRODUCTION

Cratons are extraordinary areas of continental lithosphere that have exhibited long-term stability against deformation. While the processes of their formation and preservation remain a matter of continuing enquiry, it is clear that their lithospheric structures must be so constituted as to fulfil the following two requirements throughout their history: (i) the ability to maintain a net positive balance between the opposing effects of chemical and thermal buoyancy and (ii) a total yield stress that is greater than those exerted by mantle convection. The latter, in turn, requires a thick root acquired through a cumulative process as well as high viscosity and elevated solidus by expulsion of bound molecular water. Worldwide investigations of mantle xenoliths from cratonic regions have shown that the subcrustal cratonic mantle lithosphere (SCML) consists primarily of olivine with an unusually high proportion of Mg# minerals and low Ca, Al oxides (Bernstein *et al.* 1997), even as the high Mg hosts vary from the orthopyroxene-rich harzburgites of the Kaapvaal craton (Boyd & Mertzman 1987) to the refractory dunites of Greenland

(Bernstein *et al.* 1997). However, the particular thermo-mechanical mechanism responsible for sequestering the large amounts of anhydrous lighter derivatives from the parental peridotites to form the cratonic lithosphere is a matter of debate. The two main hypotheses advanced to explain this segregation process, ones that require an efficient melting regime, assume: (i) extensive partial melting with melt and volatiles being extracted under extreme conditions within the head of a hot mantle plume and (ii) repeated reprocessing at subduction margins of the depleted oceanic mantle (Lee 2006; Arndt *et al.* 2009; Lee *et al.* 2011) which, in the Archean, would probably have a higher proportion of Forsterite, Fo#91–93. The first of these predicates a zonally differentiated pattern horizontally mediated by the distance to the plume edge and vertically by the distance above the solidus. The latter might be expected to retain the vestiges of the original stratification produced by higher levels of partial melting with decreasing depth, as well as of extensive harzburgite enrichment such as dipping interfaces of stacked oceanic mantle (Bostock 1998; Lavender *et al.* 2005). This paper presents the results of an experiment designed to discern these features in the shallow cratonic
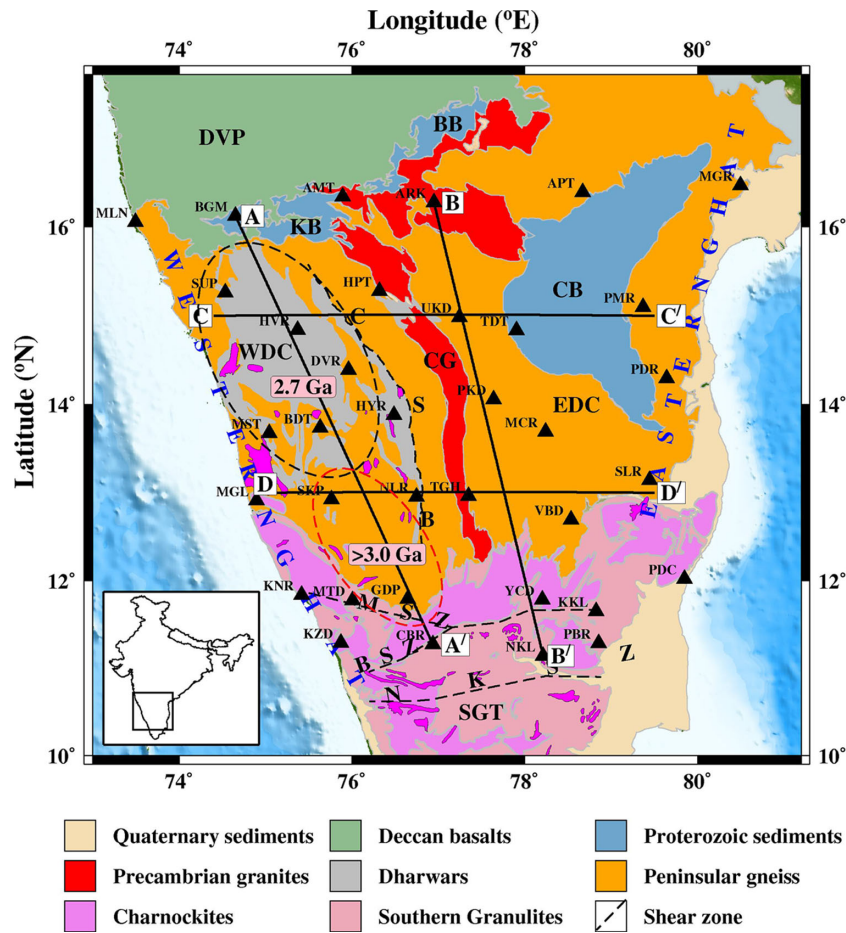
Figure 1. Major geological terrains and tectonic features of the Dharwar Craton and seismic stations (black triangles) operated in the region. EDC, East Dharwar Craton; WDC, West Dharwar Craton; SGT, Southern Granulite Terrain; DVP, Deccan Volcanic Province; CB, Cuddapah basin; KB, Kaladgi basin; BB, Bhima basin; CSB, Chitradurga Schist belt; MSZ, Moyar shear zone; BSZ, Bhavani shear zone; NKSZ, Noyil-Kavery shear zone. Dharwar schist (north) and greenstone belts (south) of the WDC are marked by black and red dashed ellipses, respectively. Shear zones are marked by black dashed lines. The thick lines corresponds to north–south (AA′, BB′) and west–east (CC′, DD′) profiles along which *Vs* variations are plotted.

mantle and to identify dissimilar parts of south India's Dharwar Craton. To do this, we analyse fundamental mode Rayleigh wave phase velocities to model the shear velocity structure of the region.

1.1 The Dharwar Craton

The Dharwar Craton is the southern constituent of the Indian Shield, thrust against a narrow belt of Eastern Ghats granulites. Stretching from 11° to 18°N, the Dharwar Craton exposes a continuum of crustal rocks bearing low-grade gneisses and greenstone basins that are fringed in the south by a 150-km-wide belt of higher grade granulites (Fig. 1) across a diffused orthopyroxene isograde. Based on age and lithology, the Western part of the Dharwar Craton (WDC) is distinguished from the Eastern (EDC) across the eastern limb of the Chitradurga Schist Belt (CSB; Naqvi & Rogers 1987). The WDC, which hosts a few enclaves of younger 2.5 Ga granites, is composed predominantly of 3.3–3.0 Ga gneisses and greenstones with the oldest (3.6 Ga) in its south-central region. The northern WDC is buried beneath the Deccan basalts but is lined at their boundary by ~2.7 Ga basins created by intermittent volcanic activity under stable conditions (Radhakrishna 1983). The southern half of the WDC shows evidence of an increasing degree of metamorphism southward by exposures of greenschist facies (3–5 Kb and 500 °C)

at 15°N to granulites (8 Kb and 800 °C), corresponding to tectonic uplift and erosion of ~5 and ~20 km, respectively.

The EDC is dominated by the late Archean (3.0–2.7 Ga) calc-alkaline complex of juvenile and anatectic granites, granodiorites and diorites (Drury *et al.* 1984; Bouhallier *et al.* 1995; Chadwick *et al.* 2000) collectively referred to as the Dharwar batholiths. It hosts the spectacular crescent-shaped Cuddappah basin (CB) that evolved around 1700 Ma through several episodes of igneous activity (Anand *et al.* 2003), and which covers more than a fifth of the area of the EDC. The region southwest of this basin is intensely pierced by east–west trending, ~2400 Ma dyke swarms (Kumar *et al.* 2012). These mafic dykes tend to fill the entire EDC (Fig. 2), a feature largely absent from the WDC. The western boundary of the CB has also been marked by occurrences of several diamond- and non-diamond-bearing kimberlites and lamproites of Proterozoic age (~1100 Ma; Chalapathi Rao 2008; Griffin *et al.* 2009).

1.2 Geophysical studies of the Dharwar Craton

There have been limited geophysical investigations of the deep structure of the Dharwar Craton. Teleseismic delay time tomography using a sparse network of analogue seismic stations brought out the existence of a ~200-km-thick lithosphere of significantly higher velocity (1–2 per cent) than the global average beneath the
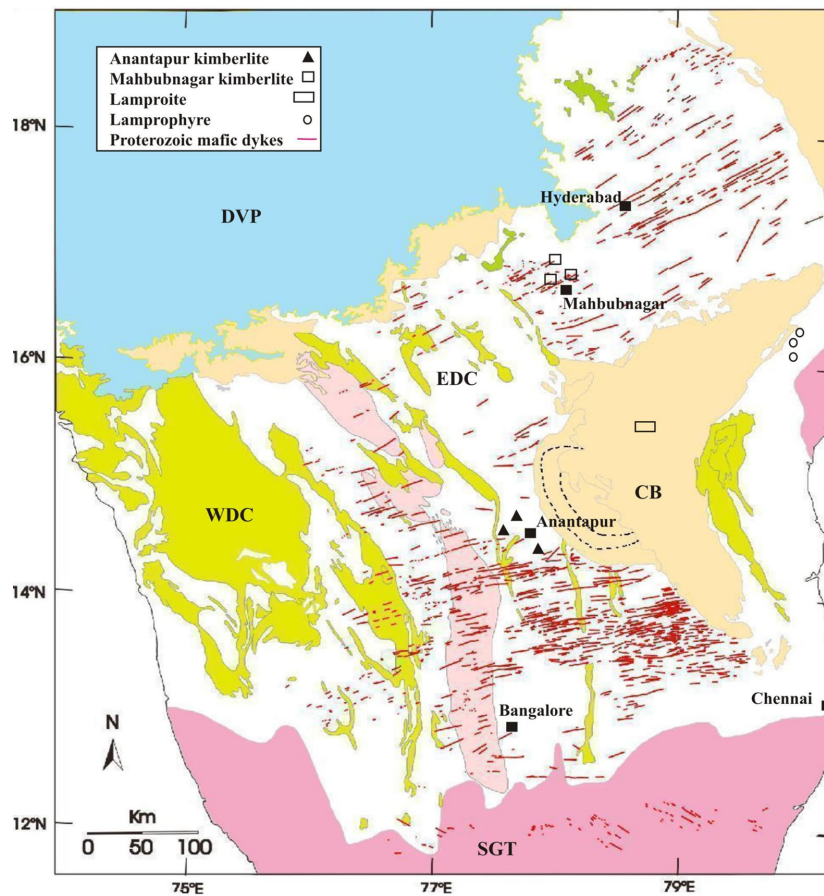
Figure 2. Location of major dyke swarms, kimberlites, lamproites and lamprophyres in the Dharwar Craton.

WDC, thinning to <100 km beneath the Eastern Ghats and the coastal basin (Srinagesh & Rai 1996; Prakasam & Rai 1998). Mitra *et al.* (2006) presented an *S*-velocity model of the Dharwar Craton determined from interstation Rayleigh wave phase velocity data. Their model showed a ~155-km-thick lithosphere composed of a two-layer crust of 35 km thickness overlying a two-layer mantle lid of 120 km thickness with an average velocity of 4.68 km s^{-1}. Their model also showed an increase in the *S* velocity at 75 km from 4.52 to 4.77 km s^{-1}. Using *S* receiver functions from three broad-band stations in the Dharwar Craton, Kumar *et al.* (2007, 2013) suggested a velocity inversion at a depth of 80–100 km which they interpreted as the base of the lithosphere, but this result was criticized by Oreshin *et al.* (2011) and Bodin *et al.* (2013) as arising from an inappropriate analysis and modelling of the data. In a recent study, Bodin *et al.* (2013) analysed data from the Geoscope station HYB in the north-central part of the Dharwar Craton using improved inversion methodology. They infer a ~200-km-thick lithosphere beneath the Dharwar Craton and a mid-lithospheric low velocity region at a depth of ~100 km. Kiselev *et al.* (2008) jointly inverted both *P* and *S* receiver functions and teleseismic *P* and *S* traveltime residuals to resolve the lithosphere–asthenosphere boundary (LAB) of the Dharwar Craton at 10 seismograph stations. The most conspicuous feature of their study is the absence of a high velocity mantle keel (*Vs* ~ 4.7 km s^{-1}), typically observed in other Archean cratons. On the other hand, they found an *S* velocity close to 4.5 km s^{-1} from the Moho down to a depth of ~250 km. Using *P* and *S* receiver functions that predominantly sample the EDC further to its east,
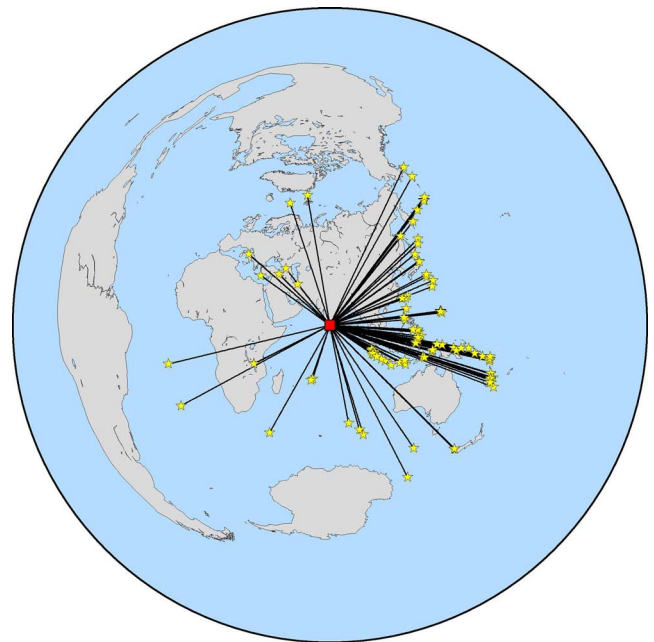

Figure 3. Locations of earthquakes (yellow star) recorded by the Dharwar seismic network (red square).

Ramesh *et al.* (2010) observed the presence of two distinct westerly dipping interfaces at depths centred at 150 and 200 km, which they interpreted as relics of Precambrian subducted slabs. Most of these studies were based on small sets of data and except for the first, were restricted to isolated geological domains.

2 PRESENT STUDY

2.1 Data analysis

Waveform data were generated at 35 broad-band seismic sites across the Dharwar Craton between 2009 February and 2011 February (Fig. 1). The spacing of the stations ranged from ~55 to ~210 km. The seismograph systems consisted of a Guralp CMG3T or 3ESP broad-band sensor recorded on a REFTEK 130 data acquisition system sampling at a frequency of 50 Hz. Seismograms for all events of $M > 5.5$ in the epicentral distance range 30° to 95° were examined for their signal-to-noise ratio, and of these, only the well-recorded (high signal-to-noise ratio) events shallower than 200 km were retained for further analysis. Most of the 113 events (Fig. 3) selected had focal depths less than 100 km, providing strong fundamental mode surface wave signals. The network produced a reasonably good azimuthal distribution of earthquakes despite most of the events occurring to the east of India (Fig. 3). The resulting ray path coverage (Fig. 4) allowed us to extract the lateral variation in the fundamental mode Rayleigh wave signals.

Rayleigh waveforms were isolated at eight periods from 20 to 80 s, after we first removed the instrument response, the trend and mean of the vertical component time-series and filtered them with a 10 mHz wide, fourth-order, double pass Butterworth filter centred
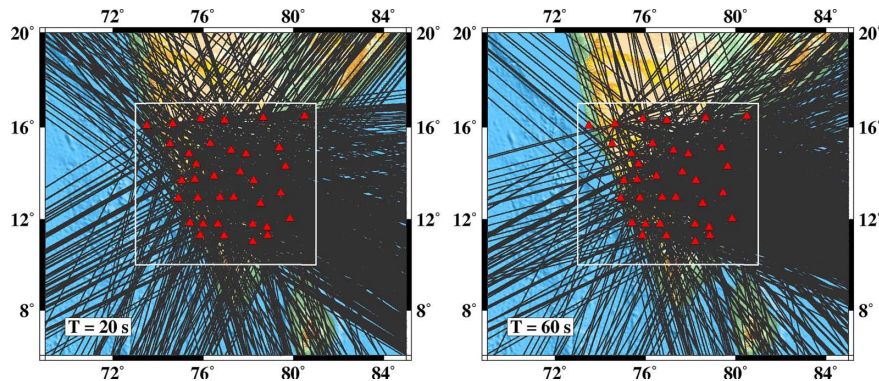

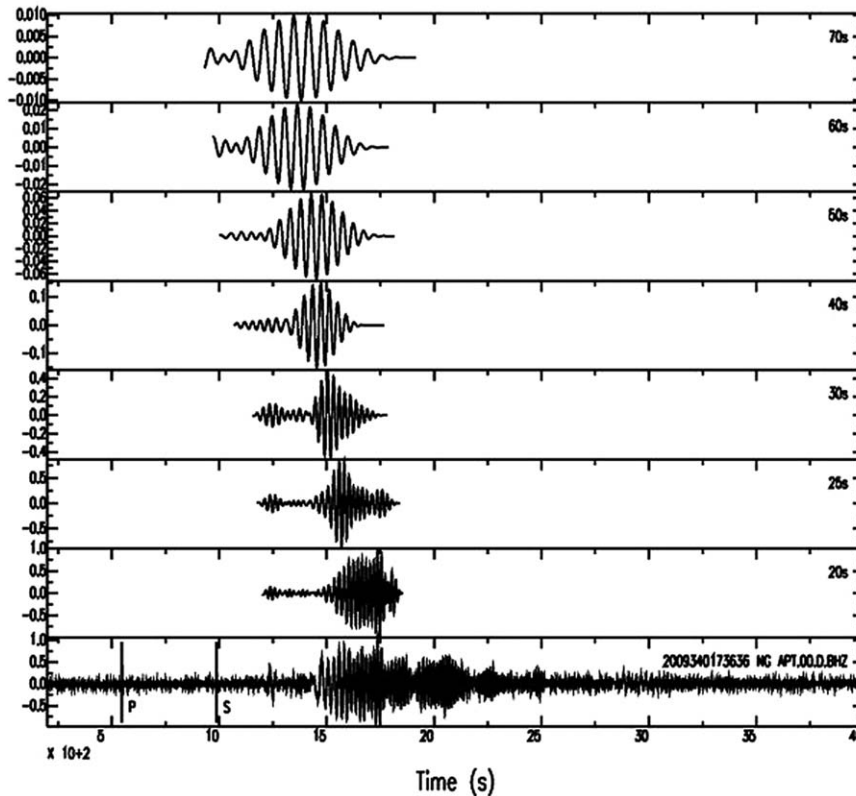**Figure 4.** Ray-path coverage for periods 20 and 60 s. Stations are marked by red triangle.

Figure 5. Vertical seismograms for station APT for an event occurred on 2009 December 6. Unfiltered seismogram is shown at the bottom and band pass filtered Rayleigh waves for periods between 20 and 70 s are presented above.
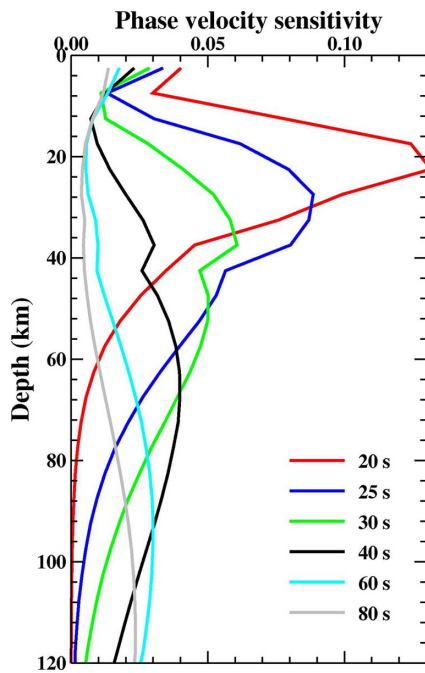
Figure 6. Phase velocity kernels for shear wave velocity for 20–80 s periods.
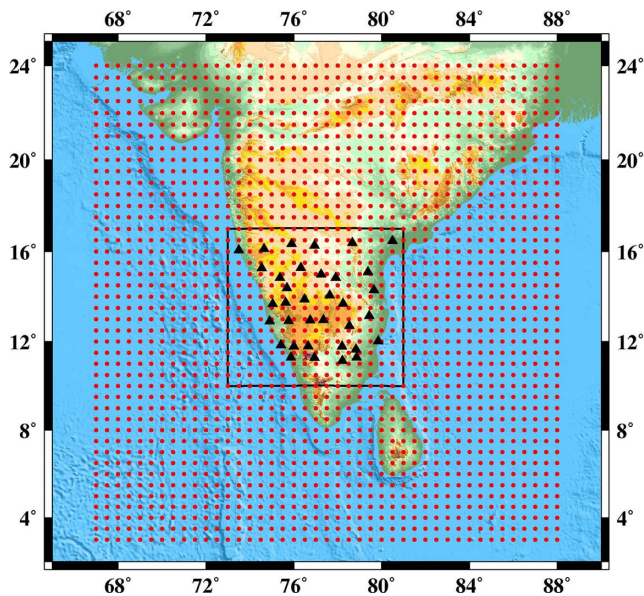

Figure 7. Grid node (red dots) parametrization and the Dharwar station location (black triangles) inside the box used in the phase velocity inversions.

at the frequency of interest. The filtered records were then windowed to isolate fundamental mode Rayleigh wave signals from other phases using window widths that captured the Rayleigh wave dispersion around the central frequency. The filtered Rayleigh wave signals were examined individually for their clarity and the selected suites were Fourier analysed to obtain their respective amplitudes and phases. An example of the original and filtered Rayleigh wave signals is shown in Fig. 5. Fig. 6 shows the effective 'sensing' depth of Rayleigh waves at the frequencies of our study.
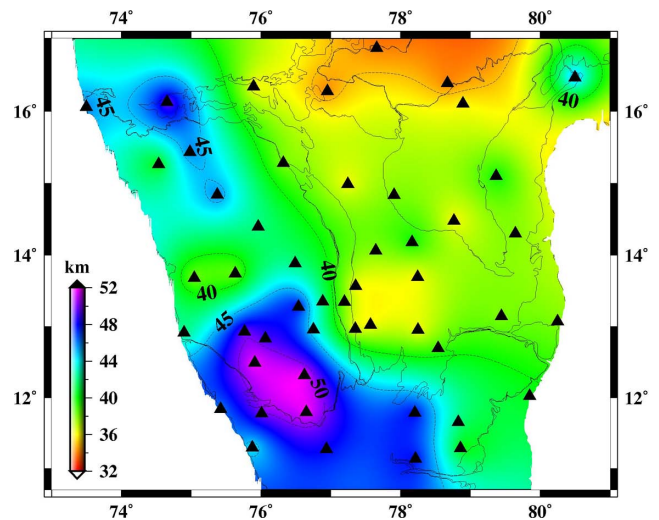

Figure 8. Moho depth variation map beneath the Dharwar Craton. Black triangles are location of seismographs (from Borah *et al.* 2014b).
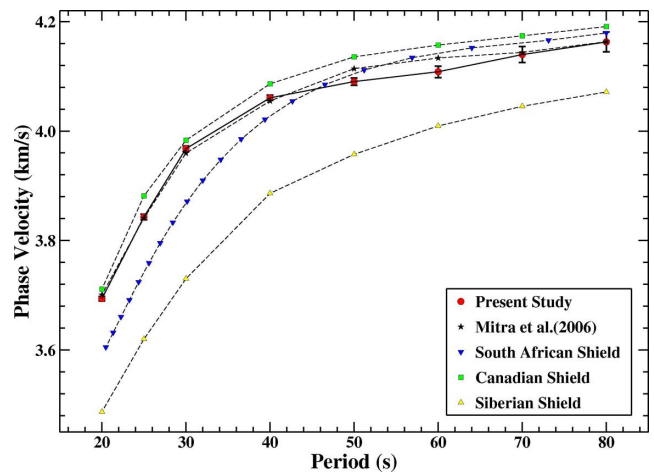

Figure 9. Average phase velocity curve of the Dharwar Craton with error bounds. Results of the other cratons (dashed line) are also shown for comparison.

2.2 Inversion for phase velocities

The determination of surface wave phase velocity assumes that the wave propagates along a great circle path and that the advancing wave front is planar across the array. This assumption is violated if velocity heterogeneities intervene this path. Non-planar energy caused by scattering or multipathing is ubiquitous and can significantly perturb the Rayleigh wave field recorded by a regional seismic network (Friederich 1999). Several approaches have been proposed to account for ray-path deviation from the idealized great circle (Friederich & Wielandt 1995; Forsyth *et al.* 1998). Forsyth *et al.* (1998) modelled the non-planar energy propagation by treating the incoming Rayleigh wavefield as a sum of two interfering plane waves with different initial phase, propagation directions and amplitudes:

$$U_z(\omega) = A_1(\omega)\exp[-i(k_1 x - \omega t)] + A_2(\omega)\exp[i(k_2 x - \omega t)],$$

$$(1)$$

where U_Z is the vertical displacement, A_i the amplitude of each incoming plane wave, k_i the horizontal wave number vectors, x the
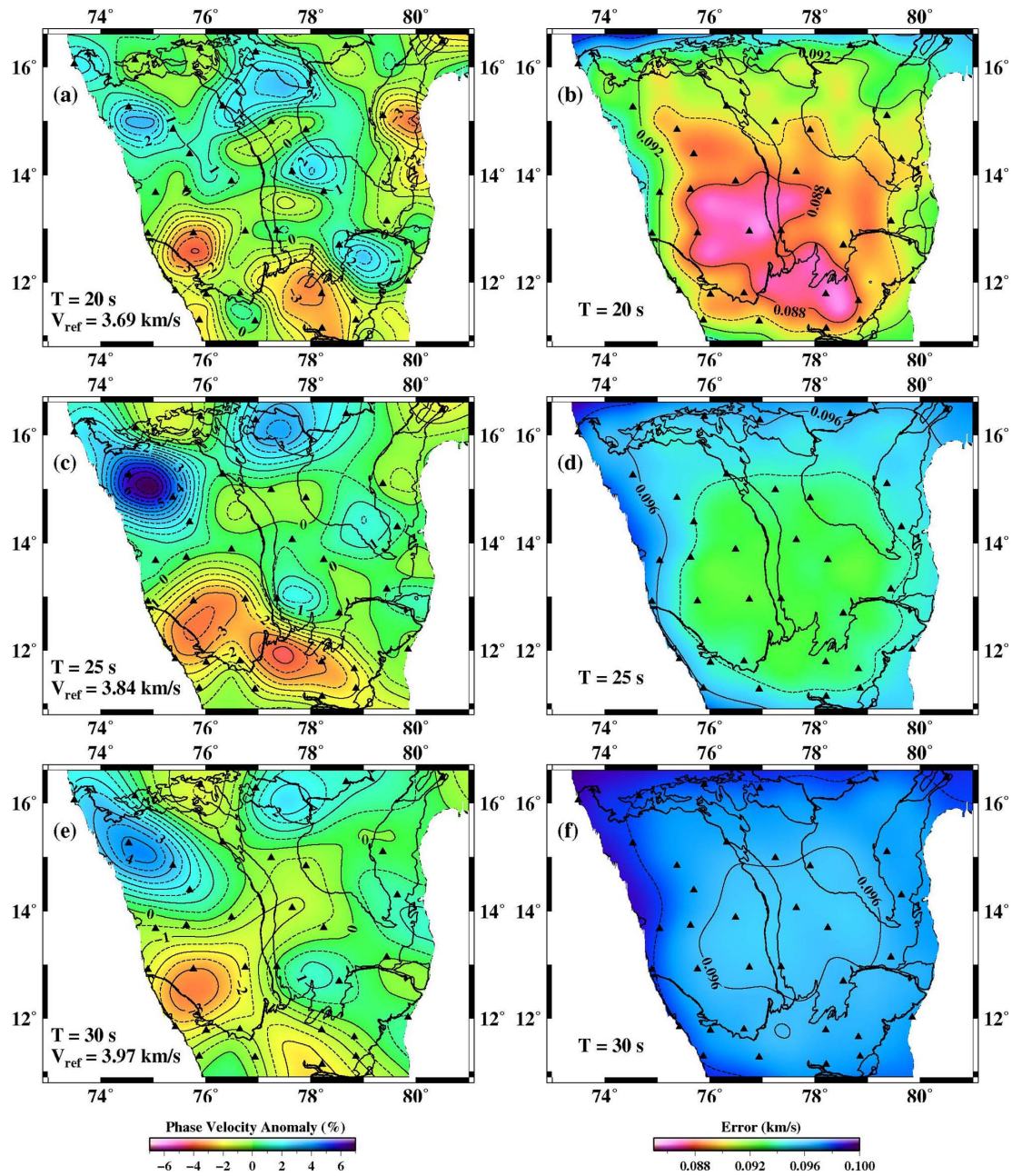
Figure 10. Rayleigh wave phase velocity maps (a, c, e, g, i, k) and standard error (b, d, f, h, j, l) with reference velocity (V_{ref}) for 20, 25, 30, 40, 60 and 80 s periods. Black triangles mark station locations. The bottom left colour scale is for the phase velocity plots and the bottom right colour scale is for the error plots.

position vector and t the time. For each event, the Rayleigh wave phases and amplitudes at all stations are normalized with respect to the station recording the largest amplitude values, assuming this is a point of constructive interference. As the wave field is represented by the sum of two plane waves with unknown amplitudes, phases and propagation directions, six parameters are required to describe the incoming wave field at each frequency.

The amplitude and phase of a Rayleigh wave at each site is determined by Fourier analysis of the filtered seismogram and the two best-fitting plane waves solved for by a simulated annealing search (Forsyth *et al.* 1998). In the second step, the data are inverted using the derived plane wave parameters and a starting phase velocity

model to obtain a phase velocity model at individual grid nodes using the Bayesian inverse:

$$\Delta m = \left(G^T C_{dd}^{-1} G + C_{mm}^{-1} \right)^{-1} \left[G^T C_{dd}^{-1} \Delta d - C_{mm}^{-1}(m - m_0) \right], \quad (2)$$

where m is the current model, m_0 the original starting model, Δm the change to the model, Δd the difference between the observed and the predicted data for the current model, G the partial derivative or sensitivity matrix relating predicted changes in d to perturbation in m and C_{dd} and C_{mm} are the *a priori* data and model covariance matrices, respectively.

To remove the influence of events that are not well described by the two-plane wave approximation, each inversion is performed in
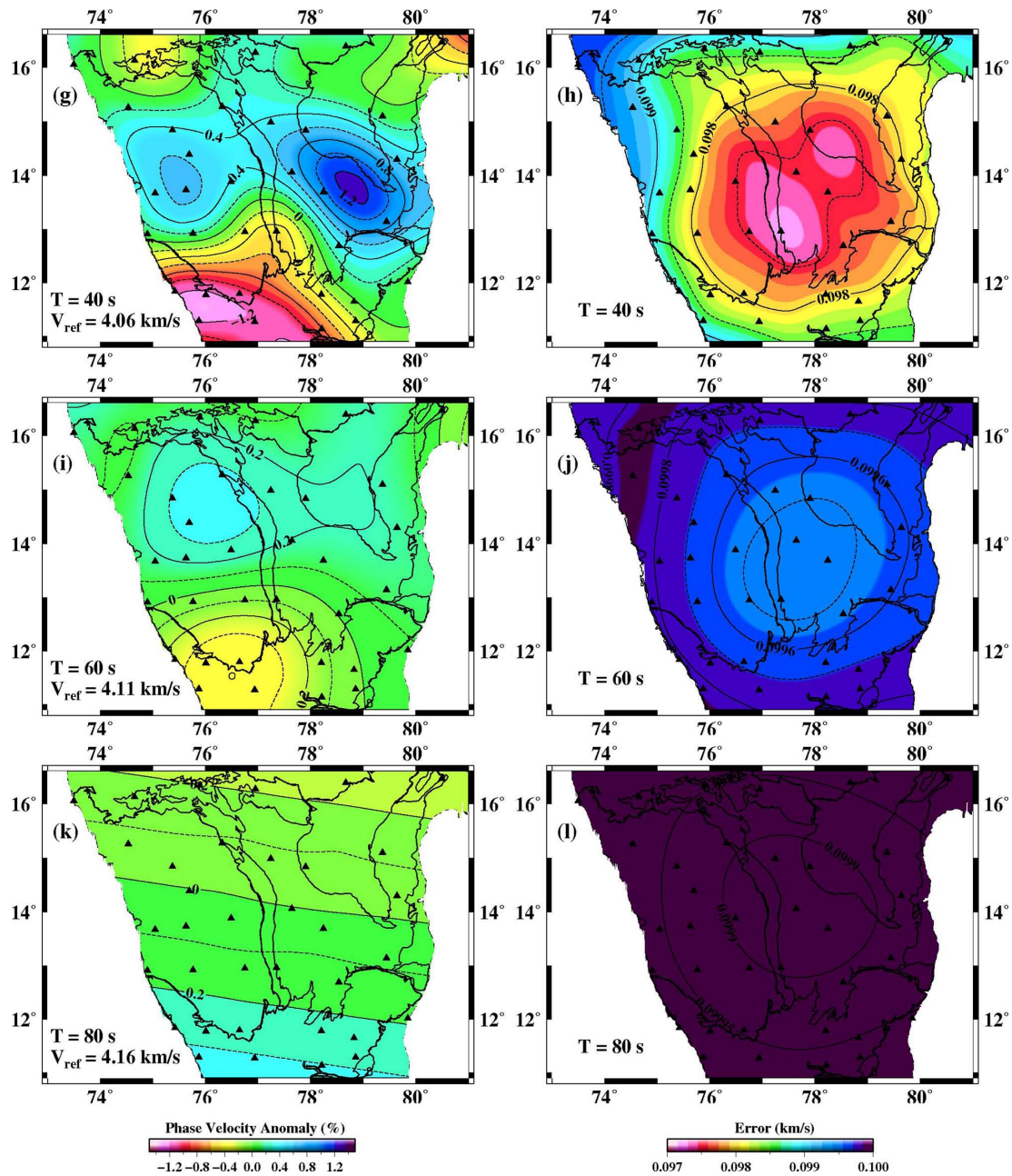
Figure 10. (*Continued*)

two stages. First, the entire set of observations are assigned equal variance and the data covariance matrix is assumed to be diagonal. A typical misfit to the normalized real and imaginary terms is of order 0.1, which we chose as the initial, *a priori* estimate of standard deviation in the first set. The inversion is terminated after 10 iterations. At this point the *a posteriori* standard deviation of the data is estimated for the individual earthquakes. In the second stage, an *a priori* standard deviation to the observations is assigned, based on the *a posteriori* standard deviations found for each event after the first set of iterations.

There is always a trade-off between resolution and variance of inverted models, that is, between the range of admissible models and misfit to the data. In the inversion for phase velocity, the resolution or regularization is governed by a combination of the smoothing length (L_w) and the *a priori* model covariance. In this study, a smoothing

length of $3\lambda/4$ was used to obtain the maximum resolution, where λ is the wavelength. We also tested smoothing lengths of λ and $3\lambda/2$. Decreasing the L_w increases both the variance of the model parameters and the amplitude of the short length scale velocity variation. Regularization is provided in the form of an *a priori* model covariance which is set to $0.1\,\mathrm{km\,s^{-1}}$.

For constructing 2-D images, the study area was paramtrized by 1856 grid nodes (Fig. 7) at $0.5°$ intervals. An *a priori* model covariance equal to 0.1 and smoothing length of ($3\lambda/4$) was assigned at each node. The surface wave phase velocity C in an isotropic medium depends only on the frequency ω and is equal to $B_0(\omega)$, where B_0 is the azimuthally averaged phase velocity (i.e. the isotropic component). For constructing a 2-D velocity image of the region, we first derived the best-fitting average phase velocity variation with period. For these inversions, the initial value of B_0 was
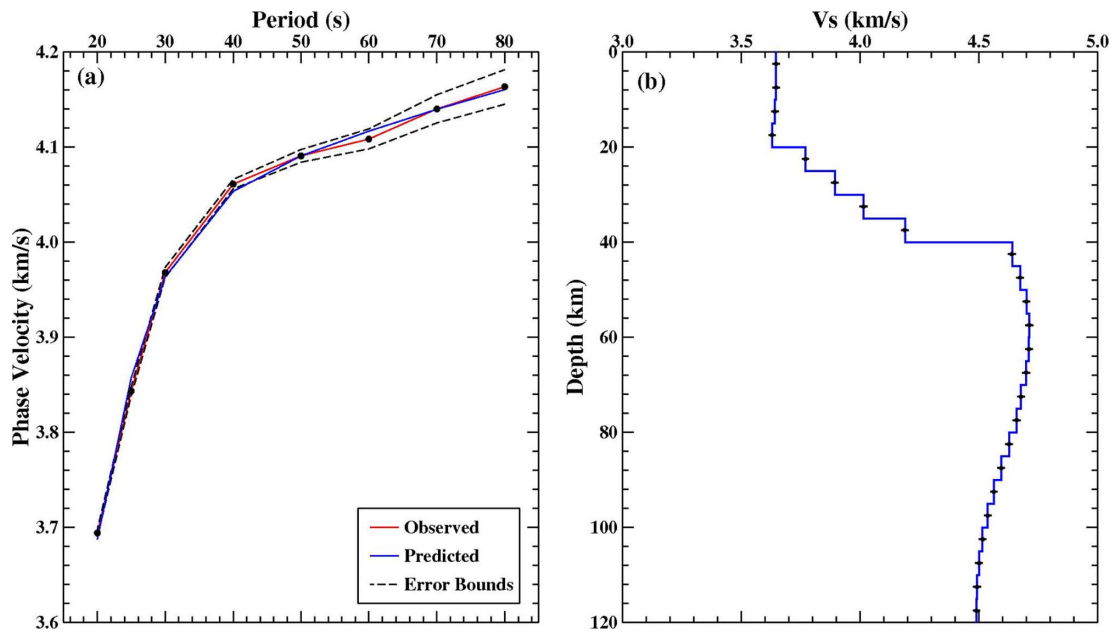
Figure 11. (a) Best-fitting dispersion curve (blue) corresponding to the (b) *Vs* model (blue). Dashed lines are the $\pm 1\sigma$ error bounds for average dispersion curve (red). Error in *Vs* model is shown by black bars.

taken from the phase velocity for the *ak135* (Kennett *et al.* 1995) velocity model. This average phase velocity model was then used as an initial value for generating the 2-D phase velocity image of the region.

2.3 Inversion for shear wave velocity

Rayleigh wave phase velocity is primarily sensitive to shear wave velocity (*Vs*) and much less influenced by the compressional wave velocity (*Vp*) and density (ρ). During the inversion the *Vp*/*Vs* value was held constant and the *P*-wave velocity updated accordingly while the density was calculated using the Nafe–Drake relation (Ludwig *et al.* 1970; Brocher 2005). Because of the large trade-off between the Moho depth and the seismic velocity structure adjacent to the Moho discontinuity, the *a priori* crustal thickness for the 1-D inversion was selected from the results of earlier investigations. Early wide-angle reflection and refraction records across the central part of this craton suggest that the crust is broken into blocks with distinct Moho depths varying from 34 km in the east to 41 km in the west (Kaila *et al.* 1979; Roy Chowdhury & Hargraves 1981). Receiver function studies (Gupta *et al.* 2003; Rai *et al.* 2013; Borah *et al.* 2014a,b) show significant variations in the Moho depth beneath the Dharwar Craton: ~34–38 km in the EDC, ~38–46 km in the Eastern and Western Ghats, and 40–50 km beneath the Southern Granulite Terrain (SGT). Below the WDC, the Moho depth increases from ~38–46 km in the north to ~44–52 km in the south. Fig. 8 shows the Moho variability beneath the Dharwar Craton. An average Moho depth of 40 km was, therefore, selected as an initial crustal thickness for the 1-D shear wave velocity inversion. The model consists of a stack of 5 km-thick layers composed of 20 km of upper crust (*Vs* = 3.49 km s^{-1}) and four layers of lower crust (shear wave velocities: 3.65, 3.8, 3.95 and 4.15 km s^{-1}) overlying the reference velocity model *ak135* from 40 km (Moho) to 200 km depth, The average phase velocity data were inverted in terms of a 1-D shear wave velocity–depth profile using the routine of Herrmann & Ammon (2004). The resulting best 1-D average shear wave

velocity model was subsequently used as an initial model to generate the *Vs*-depth profile at different locations in the region. These 1-D shear wave velocity models were eventually gathered to construct a 3-D shear wave velocity model.

3 RESULTS

3.1 Phase velocity computation

Only a few paths have phase velocity measurements with high signal-to-noise ratio for periods greater than 80 s and we restrict our study to this maximum period. Below 30 s period, surface waves are primarily influenced by crustal structure and at 40 s period they begin to 'sense' the upper mantle structure. We first create a mean phase velocity curve for the Dharwar Craton from the first stage of the two-plane wave inversion. The mean phase velocities vary from 3.69 km s^{-1} at 20 s to 4.16 km s^{-1} at 80 s, with standard deviations between 0.004 and 0.018 km s^{-1} (Fig. 9). Fig. 9 also compares the fundamental mode average phase velocity curve for the Dharwar Craton with those from other shields. Dispersion values for the Dharwar Craton are higher than those for the Siberian (Priestley & Debayle 2003) and South African Shields (Priestley 1999), but lower than the Canadian Shield (Brune & Dorman 1963). The lower phase velocities for the Siberian Shield compared to those of others shields is probably due to the thicker crust (45 km) of the Siberian Shield compared to the other shields. A small variation is observed in the dispersion curve at 50–60 s between our mean curve for the Dharwar Craton and the results of Mitra *et al.* (2006), but this is probably due to the wider region covered by our study.

Using the average phase velocity as a starting point, we computed the phase velocity dispersion curves at each grid node (0.5° × 0.5°; Fig. 7), keeping the damping (0.1) and smoothing length (3λ/4) the same as in the 2-D inversion. Variations of phase velocities at periods from 20 to 80 s are shown in Fig. 10 (left-hand panel) along with their associated errors (right-hand panel) estimated from
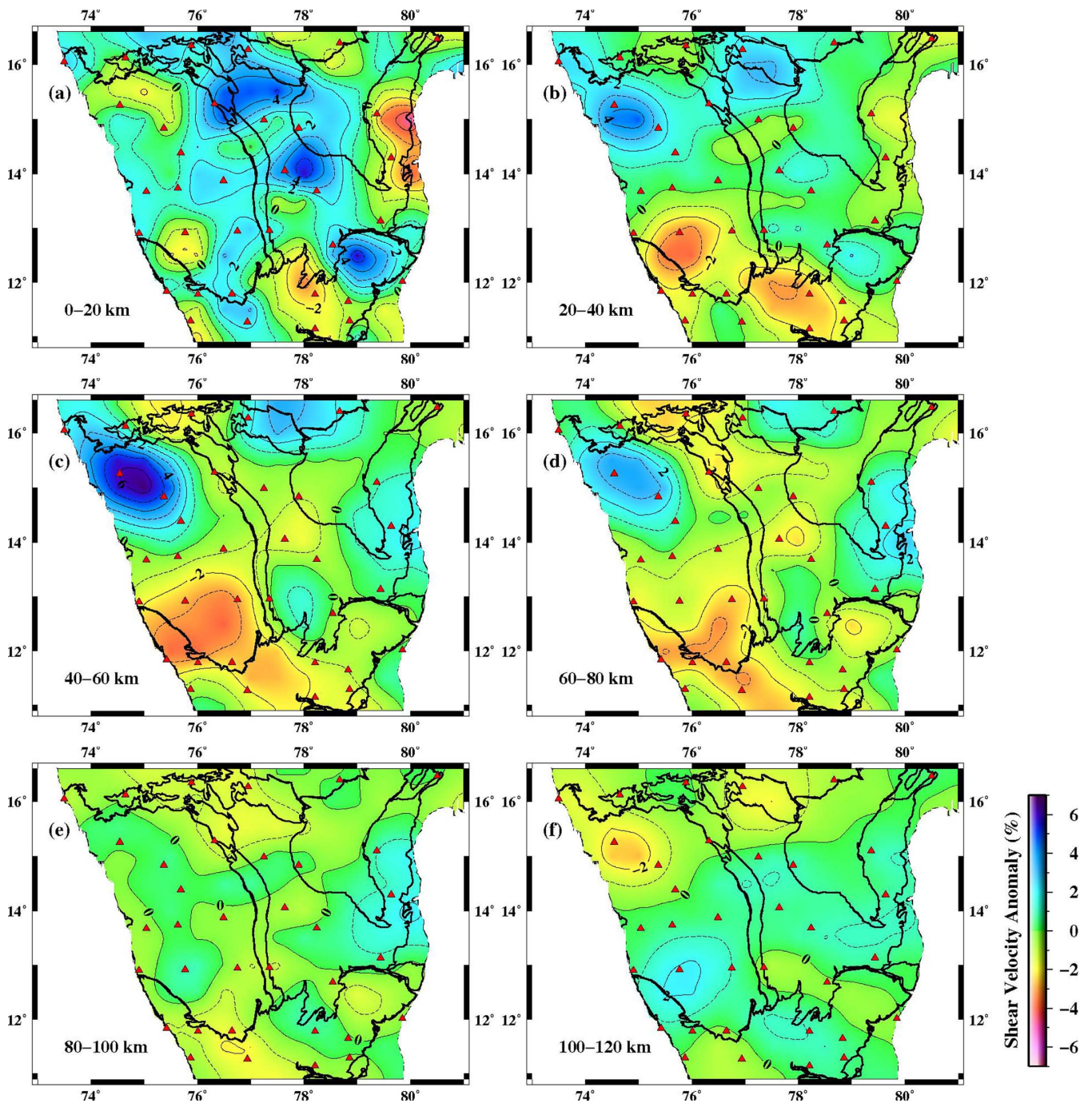
Figure 12. Average shear velocity anomaly in different depths ranges (a) 0–20 km, (b) 20–40 km, (c) 40–60 km, (d) 60–80 km, (e) 80–100 km and (f) 100–120 km. Stations are marked by red triangles.

model covariance matrices and the weighting function. The colour code has been shifted after 30 s period to account for the phase velocity variation. All error maps (right-hand panel in Fig. 10) show a similar pattern, with increasing error values from the centre to the edge of the study area. Due to overlapping sampling depths, the phase velocity maps show gradual changes among adjacent periods. At 20 s period, which primarily senses the crust, the southern part of WDC and SGT show low phase velocities, ones that are visible at all periods but in diminishing degree with increasing periods. This could be a consequence of the thickened crust that has been

mapped using receiver functions (Gupta *et al.* 2003; Rai *et al.* 2013; Borah *et al.* 2014a,b). At longer periods a significant high velocity anomaly is observed in the northern WDC; this section of the WDC also contains prominent deposits of iron and manganese ores. Most parts of the EDC show a small positive anomaly for all periods without any characteristic features. The results are tested by repeating the *Vs* inversions with varying smoothing length of λ and 3λ/2. Tomographic results obtained for those values were found to be of similar geometry to those obtained for a smoothing length of 3λ/4 but with a change in amplitude.
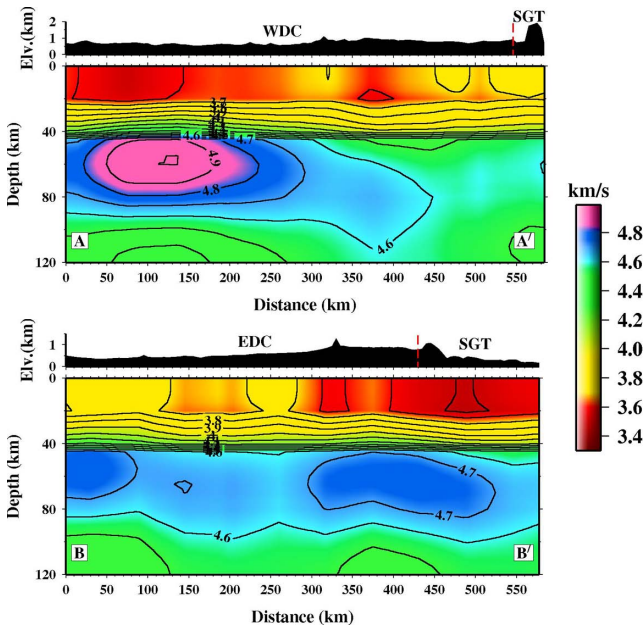
Figure 13. Absolute shear wave velocity cross-section (N–S) with topography on the top along the two profiles (shown in Fig. 1). Profile AA$'$ and BB$'$ pass through the WDC and the EDC in north to SGT in south. Red dashed lines indicate the location of tectonic boundaries.
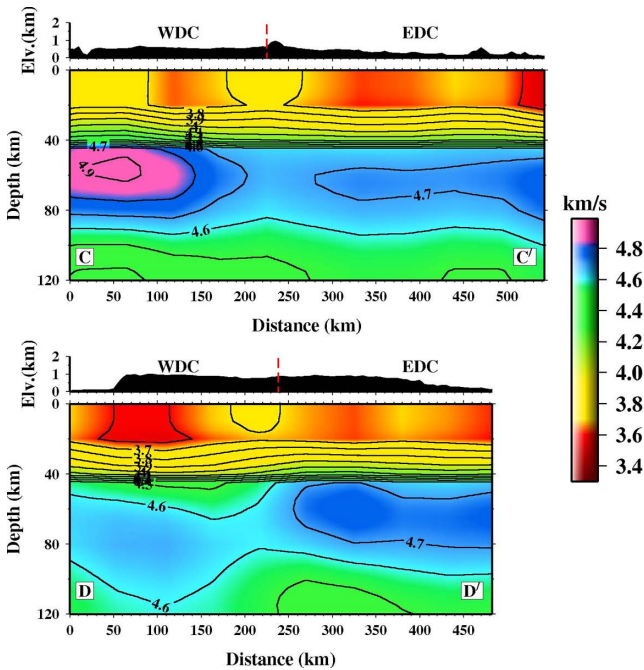
Figure 14. Absolute shear wave velocity cross-section (W–E) with topography on the top along the two profiles (shown in Fig. 1). Profile CC$'$ and DD$'$ pass through north and south part of the WDC and the EDC respectively. Red dashed lines indicate the location of tectonic boundaries.

3.2 3-D shear velocity model

We then invert the average phase velocity for the region (Figs 9 and 11a) for an average upper mantle velocity model of the Dharwar Craton (Fig. 11b). This model has a high velocity upper mantle lid (4.6–4.7 km s^{-1}) extending to ~100 km depth. We then used the phase velocity values determined at individual grid points to invert for the lateral variation in shear velocity (Vs), depth, using the

average shear velocity for the Dharwar Craton (Fig. 11b) as a starting point. A 3-D shear velocity model for the region was then created by gathering all 1-D shear velocities from 0.5° gridpoints (Fig. 7). The shear wave velocity in different depth ranges (Fig. 12) relative to the average 1-D wave velocity reveals lateral inhomogeneities (−2 per cent to 8 per cent) beneath the Moho to a depth of 100 km, the most remarkable being the high +8 per cent (Vs ~4.9 km s^{-1}) shear wave anomaly in the northern WDC. This feature is also prominent in the phase velocity map. In this same depth range, however, the southern part of the WDC shows lower wave speeds. At levels deeper than 100 km, the lateral inhomogeneity is significantly reduced (±1 per cent). However, the shallower mantle velocity in the EDC is close to the average for the region.

3.2.1 Velocity sections

Cross-sections of the absolute shear wave velocity model along N–S and W–E profiles are shown in Figs 13 and 14, respectively. Along the N–S section AA$'$, the shear wave speed at ~50–80 km depth varies from 4.9 km s^{-1} below the northern part of the WDC to 4.6 km s^{-1} below the southern part of the WDC. At deeper depths beneath the whole of the WDC, the wave speed is ~4.5 km s^{-1}, close to the global average at these depths. Beneath the EDC (section BB$'$), a high velocity lid with a shear wave speed of ~4.6–4.7 km s^{-1} occurs. Along the E-W profile CC$'$, a 50-km-thick high shear wave speed layer exists below the Moho from the WDC to the EDC with the wave speed decreasing from west to east. Along profile DD$'$ a high wave speed (~4.6 km s^{-1}) layer occurs down to a depth of ~110 km in the southern WDC which becomes shallow eastward in the southern EDC to ~90 km. These results show that a high velocity lid with varying velocity and thickness exists beneath the whole of the craton.
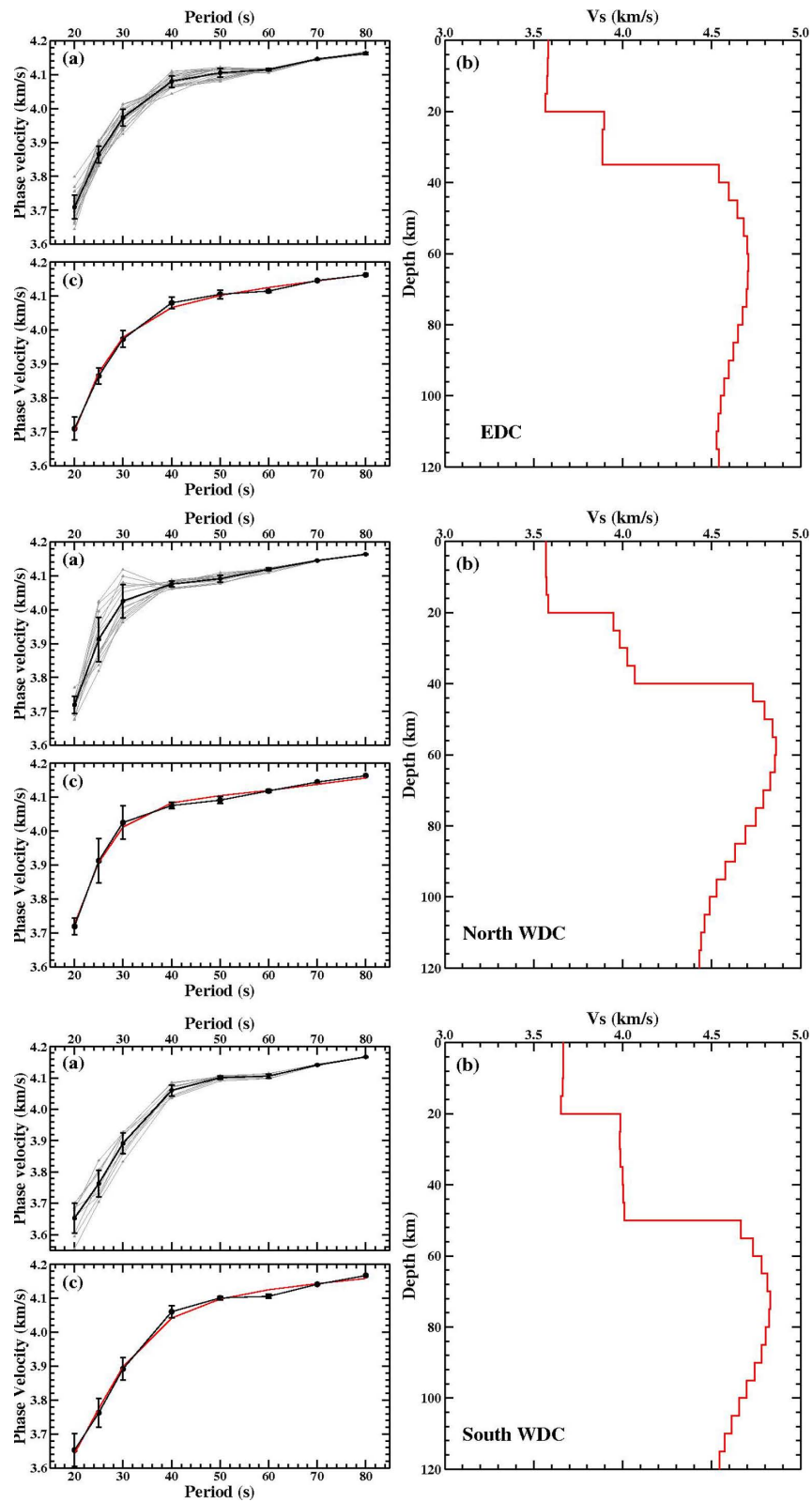
3.2.2 Average shear velocity model for the EDC and the WDC

We identify three distinct regions within the Dharwar Craton: the northern WDC, the southern WDC and the EDC. We calculated the mean phase velocity curves for these blocks and inverted them for their shear wave speed structure. The mean phase velocities for each block were determined by averaging the values at the grid points in each of the blocks as follows:

$$V_{ew}^{j} = \sum_{i=1}^{n} \left(V_{i}^{j} / E_{i}^{j} \right) / \sum_{i=1}^{n} \left(1/E_{i}^{j} \right), \tag{3}$$

where V_{ew}^{j} is the error-weighted phase velocity for the jth period, V_i the phase velocity for the ith dispersion curve and the jth period and E_i the associated phase velocity error. We then computed the ±1 standard deviation bounds for the average phase velocity at each period (Fig. 15a). We used the average 1-D shear velocity model for the Dharwar Craton but with average Moho depths for the three regions determined by receiver function analysis (35 km for the EDC, 40 km for the northern WDC, 50 km for the southern WDC) for an initial model and inverted the dispersion data for the shear wave speed structure down to a depth of 120 km (Fig. 15b). The dispersion curves computed from these models provide an excellent fit to the observed dispersion data (Fig. 15c).

We compare the phase velocities for three blocks and the phase velocity for global models *PEM-C* (Dziewonski *et al.* 1975) and *ak135* in Fig. 16(a). Dispersion curves for the three blocks of the Dharwar Craton show significant variations between 20 and 40 s periods. Beyond 40 s, they are similar but much higher than those

Figure 15. Average phase velocities and average shear velocity models for the EDC, north WDC and south WDC. (a) Error weighted phase velocities with error bounds (black line). Grey lines are the dispersion curves in the block. (b) *Vs* model which fit the dispersion curve. (c) Computed phase velocity dispersion curve (red line) and the observed one (black line).
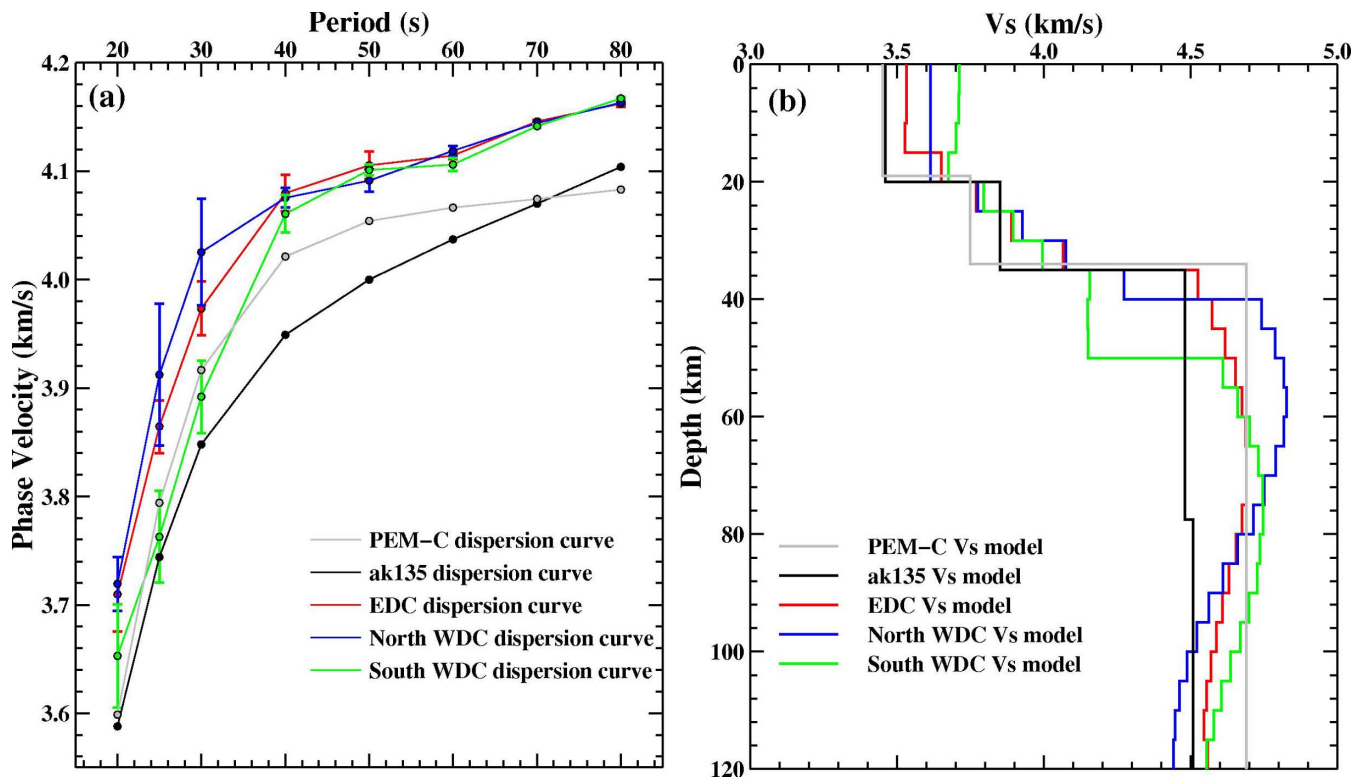
Figure 16. (a) Average phase velocity dispersion curves for the block EDC, north WDC and south WDC along with *PEM-C* and *ak135* phase velocities. (b) Average shear velocity models for the block EDC, north WDC and south WDC along with *PEM-C* and *ak135* shear velocity model.

of the global average. Phase velocities at all periods for the northern WDC and the EDC blocks are significantly higher than the dispersion for *PEM-C* and *ak135*. For the southern WDC, they are similar to the dispersion of *PEM-C* and *ak135* up to 30 s period but increase significantly at higher periods. Shear velocity models for the three blocks along with that for *PEM-C* and *ak135* model are compared in Fig. 16(b). These show that below the Moho down to a depth of ∼100 km, *Vs* in the Dharwar Craton is significantly higher (by 0.2–0.4 km s^{-1}) compared to the *Vs* of the global average models but similar at deeper levels.

To establish the reliability of the shear velocity model, that is, the existence of a high velocity layer (4.7–4.9 km s^{-1}) in the shallow mantle followed by velocity reduction (4.5 km s^{-1}) in the three blocks (EDC, north WDC and south WDC), we tested various forward models. We find that the inverted shear velocity model (with Moho at 35 km) for the EDC block (red line in Fig. 17b) fits the dispersion curve rather well (red line in Fig. 17a). Changing shear velocity values in the shallower mantle to 4.53 and 4.7 km s^{-1}, leads to dispersion values significantly lower and higher than in the observed phase velocities. Similar tests for the other two blocks show the same result.

We further demonstrate the robustness of shear velocity result due to change in crustal thickness or velocity contrast at the Moho. We varied the Moho depth by ±5 km with reference to the initial model of Moho depth 40 km and inverted the shear velocity model for north WDC. The resulting inversion results for the three Moho models show similar results (Fig. 18a). Similarly, we varied the velocity contrast at Moho by ±4 per cent compared to the initial model and inverted the velocity model for north WDC (Fig. 18b). We observe very small difference in the resulting velocity models.

4 DISCUSSIONS AND CONCLUSIONS

The shear wave velocity model of the Dharwar Craton determined from the inversion of fundamental mode Rayleigh wave phase velocities distinguishes an upper ∼50-km-thick high wave speed upper mantle lid of shear wave velocity 4.6–4.9 km s^{-1} overlying a deeper layer of shear wave velocity ∼4.5 km s^{-1}, which is near the global average shear wave velocity at these depths. Although the frequency range of our data limits our investigation to depths of ∼120 km, this lower layer probably continues deeper to the LAB, which is about 170 km in southern India (Mitra *et al.* 2006; Priestley & McKenzie 2013).

Shear wave velocities in the Earth vary with temperature and composition. A 100°K change in temperature leads to ∼5 per cent change in shear velocity, while differences in composition are generally responsible for 1 per cent velocity variation (Priestley & McKenzie 2006, 2013; Schutt & Lesher 2006). From a geotherm based on xenolith data from EDC, Roy & Mareschal (2011) calculated mantle shear velocities and found these to be less than the global model values (Shapiro & Ritzwoller 2002). This result emphasizes the significance of compositional variations in explaining the observed anomalies and their implications to craton formation processes.

The mantle stratification delineated by the *Vs* anomalies at ∼100 km depth beneath the Dharwar Craton is consistent with the isopycnic lithosphere proposed by Jordan (1988) who argued that the continued preservation of a cratonic lithosphere against convective stresses through a temporally cooling Earth of increasing viscosity required the compositional and thermal buoyancy to be balanced at every depth in the lithosphere. The lower lithosphere is at nearly the same temperature as the surrounding asthenosphere,
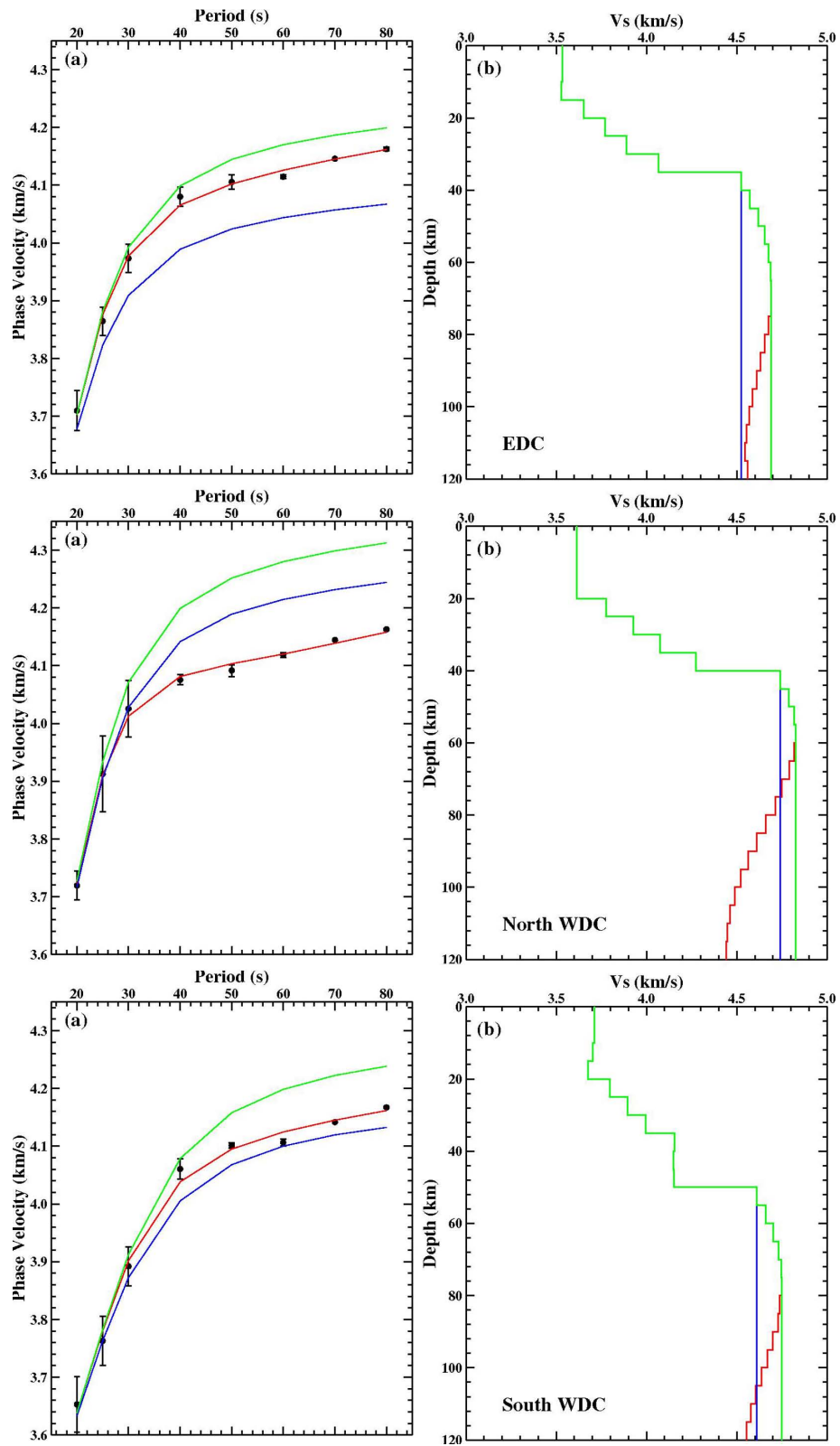
Figure 17. Reliability check for the shear velocity models of the Dharwar Craton. Figure shows, dispersion curve (a) computed for different velocity models (b). Black circles are the observed phase velocity dispersion with $\pm 1\sigma$ error bounds.
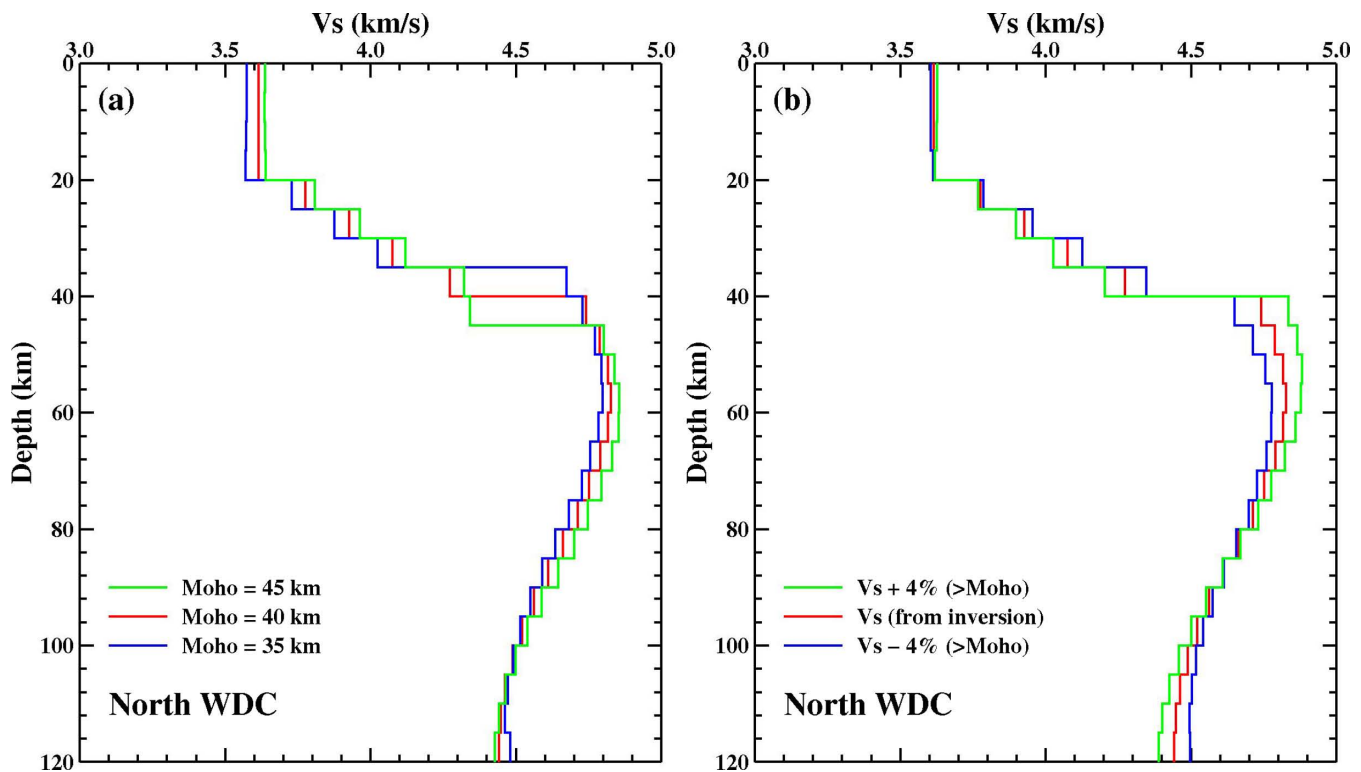
Figure 18. Analysis of robustness of shear velocity result due to change in (a) Moho depth (40 km) by ±5 km and (b) *Vs* by ±4 per cent at Moho.

and would, therefore, resist foundering, even with the marginal compositional buoyancy as that offered by the less-depleted lherzolite residues at the base of a melting column.

However, the range and lateral distribution of the positive anomalies in the Dharwar upper mantle are remarkable. While being positive nearly everywhere, this high velocity marks the northwestern craton with an unusually high anomaly of 8 per cent that is an extremely high shear wave velocity of 4.9 km s^{-1}. The existence of higher velocity, lighter refractory materials in the upper cratonic mantle, is of course, a necessary condition for its longevity, as borne out by the prevalence of positive velocity anomalies throughout the craton between 50 and 100 km depth. But, the existence of an extraordinarily depleted region of ∼100 km radius suggests that it evolved in the highest column of an intensively melting plume.

Two notable features of this anomalous upper mantle are the wide variation in the magnitude of the anomalies and a very sparse distribution of moderately conspicuous anomalies. Furthermore, there is little coherence in their geographical patterns, suggesting that the craton was finally assembled from individually evolved units of lateral extents comparable to their depths. Yet, this raises tantalizing questions about the processes that mediated their amalgamation by the late Archean. One could, for example, model the possible compositions of the northwestern cratonic upper mantle distinguished by its high anomaly to test whether or not its origin is compatible with the result of plume melting. This should, in turn, provide constraints on the dimensions of a plume sustainable by an Archean mantle as well as limits on plume activity required to generate the feeblest craton.

Finally, it is tempting to relate the structure of the shallow upper mantle of the Dharwar Craton to that of its crust as described by

Borah *et al.* (2014a,b) who reported a wide variation (36–52 km) in the thickness of its eastern and western constituents. The EDC was found to have a characteristic flat Moho at ∼36 km with an average crustal *Vs* of ∼3.7 km s^{-1}, whereas the northern and the southern WDC had variable Moho depths, respectively, of ∼38–46 km with an average *Vs* ∼3.8 km s^{-1}, and 44–52 km with an average *Vs* of 3.9 km s^{-1}. Since the region has a nearly flat topography with elevations of only 500–800 m above mean sea level, this wide range in Moho depths of the WDC cannot be explained by simple isostatic compensation and provides an interesting context in which to model the densities of the Dharwar crust and upper mantle. The thicker crust beneath the WDC is also marked by higher *Vs* (4.7–4.9 km s^{-1}) in the shallow mantle and near-absence of mafic dyke swarms which pervasively dissect the EDC. The latter, with a nearly flat Moho, is underlain by a shallow mantle of relatively more homogeneous and lower *Vs*, ∼4.5–4.7 km s^{-1}, suggesting that it was most likely homogenized by tectono-thermal event(s) subsequent to its cratonization. Several prominent surface features of the EDC are more likely associated with such a hypothetical event (Fig. 2). However, much more research is required to consolidate these observations of the various cratonic columns into a plausible, testable hypothesis.

ACKNOWLEDGEMENTS

and forms part of his PhD dissertation. We are thankful to staff of the seismic tomography project at CSIR-NGRI for their support in execution of the field programs. This is Cambridge University Department of Earth Sciences contribution 3031. We thank the editor, Prof. Michael Ritzwoller and both the reviewers (Derek Schutt and anonymous) for their valuable suggestions for improve the paper.

REFERENCES

Anand, M., Gibson, S.A., Subbarao, K.V., Kelley, S.P. & Dickin, A.P., 2003. Early Proterozoic melt generation processes beneath the Intra-cratonic Cuddapah Basin, Southern India, *J. Petrol.,* **44,** 2139–2171.

Arndt, N.T., Coltice, N., Helmstaedt, H. & Gregoire, M., 2009. Origin of Archean subcontinental lithospheric mantle: some Petrrological constraints, *Lithos,* **109,** 61–71.

Bernstein, S., Keleman, P.B. & Brook, C.K., 1997. Highly dpleted spinel harzburgite xenoliths in Tertiary dykes from East Greenland, *Earth planet. Sci. Lett.,* **154,** 221–235.

Bodin, T., Yuan, H. & Romanowicz, B., 2013. Inversion of receiver functions without deconvolution—application to the Indian Craton, *Geophys. J. Int.,* **196,** 1025–1033.

Borah, K., Rai, S.S., Gupta, S., Prakasam, K.S., Sivaram, K. & Sudesh, Kumar, 2014a. Preserved and modified mid-Archean crustal blocks in Dharwar craton: Seismological Evidence, *Precambrian Res.,* **246,** 16–34.

Borah, K., Rai, S.S., Prakasam, K.S., Gupta, S., Priestley, K. & Gaur, V.K., 2014b, Seismic imaging of crust beneath the Dharwar craton, Inda, from ambient noise and teleseismic receiver function modelling, *Geophys. J. Int.,* **197,** 748–767.

Bostock, M.G., 1998. Mantle stratigraphy and the evolution of the Slave province, *J. geophys. Res.,* **103,** 21 183–21 200.

Bouhallier, H., Chardon, D. & Choukroune, P., 1995. Strain patterns in Archean dome and basin structures; the Dharwar craton (south India), *Earth planet. Sci. Lett.,* **135,** 57–175.

Boyd, F.R. & Mertzman, S.A., 1987. Composition and Structure of the Kaapvaal lithosphere, southern Africa in *Magmatic Processes: Physico-Chemical Principles,* Vol. 1, pp. 13–24, ed. Mysen, B.O., Geochem. Society Spl. Publication.

Brocher, T.M., 2005. Empirical relations between elastic wave speeds and density in the Earth's crust, *Bull. seism. Soc. Am.,* **95,** 2081–2092.

Brune, J.N. & Dorman, J., 1963. Seismic waves and earth structure in the Canadian Shield, *Bull. seism. Soc. Am.,* **53,** 167–210.

Chadwick, B., Vasudev, V.N. & Hegde, G.V., 2000. The Dharwar Craton, southern India, interpreted as a result of Late Archean oblique convergence, *Precambrian Res.,* **99,** 91–111.

Chalapathi Rao, N.V., 2008. Petrophysical properties of Indian Kimberlites, Lamproites and lamprophyres, in *Indian Dykes- Geochemistry, Geophysics and Geochronology,* pp. 309–318, Narosa Pub., N. Delhi.

Drury, S.A., Harris, N.B., Holt, R.W., Reeves-Smith, G.J. & Wightman, R.T., 1984. Precambrian tectonics and crustal evolution in south India, *J. Geol.,* **92,** 3–20.

Dziewonski, A.M., Hales, A.L. & Lapwood, E.R., 1975. Parametrically simple earth models consistent with geophysical data, *Phys. Earth planet. Int.,* **10,** 12–48.

Forsyth, D.W., Web, S.C., Dorman, L.M. & Shen, Y., 1998. Phase velocities of Rayleigh waves in the MELT experiment on the East Pacific Rise, *Science,* **280,** 1235–1238.

Friederich, W.E. & Wielandt, E., 1995. Interpretation of seismic surface waves in regional networks: joint estimation of wavefield geometry and local phase-Methods and tests, *Geophys. J. Int.,* **120,** 731–744.

Friederich, W.E., 1999. Propagation of seismic shear and surface waves in a laterally heterogeneous mantle by multiple forward scattering, *Geophys. J. Int.,* **136,** 180–204.

Griffin, W.L., Kobussen, A.F., Babu, E.V.S.S.K., O'Reilly, S.Y., Norris,

R. & Dengupta, P., 2009. A translithospheric suture in the vanished 1-Ga lithospheric root of South India: evidence from contrasting lithosphere sections in the Dharwar Craton, *Lithos,* **112**(Supp. 2), 1109–1119.

Gupta, S., Rai, S.S., Prakasam, K.S., Srinagesh, D., Bansal, B.K., Chadha, R.K., Priestley, K. & Gaur, V.K., 2003. The nature of the crust in southern India: Implication for Precambrian crustal evaluation, *Geophys. Res. Lett.,* **30,** 1419, doi:10.1029/2002GL016,770.

Herrmann, R.B. & Ammon, C.J., 2004. Surface wave, receiver function and crustal structure, *Computer Programs in Seismology,* version 3.30, St. Louis University.

Jordan, T.H., 1988. Structure and formation of the continental tectosphere, *J. Petrol.,* **Special_Volume**(Special Lithosphere issue), 11–37.

Kaila, K.L. *et al.*, 1979. Crustal structure along Kavali-Udipi profile in the Indian peninsular shield from deep seismic soundings, *J. Geol. Soc. Ind.,* **20,** 307–333.

Kennett, B.L.N., Engdahl, E.R. & Bulland, R., 1995. Constraints on seismic velocities in the Earth from travel times, *Geophys. J. Int.,* **122,** 108–124.

Kiselev, S., Vinnik, L., Oreshin, S., Gupta, S., Rai, S.S., Singh, A., Kumar, M.R. & Mohan, G., 2008. Lithosphere of the Dharwar craton by joint inversion of P and S receiver functions, *Geophys. J. Int.,* **173,** 1106–1118.

Kumar, A., Hamilton, M.K. & Halls, H.C., 2012. A Paleoproterozoic giant radiating dyke swarm in the Dharwar Craton, southern India, *Geochem., Geophys. Geosys.,* **13,** doi:10.1029/2011GC003926.

Kumar, P., Yuan, X., Ravi Kumar, M., Kind, R., Li, X. & Chadha, R.K., 2007. The rapid drift of the Indian tectonic plate, *Nature,* **449,** doi:10.1038/naturee06214.

Kumar, P., Kumar, M.R., Srijayanthi, G., Arora, K., Srinagesh, D., Chadha, R.K. & Sen, M.K., 2013. Imaging the lithosphere-asthenosphere boundary of the Indian Plate using converted wave techniques, *J. geophys. Res.,* **118,** 1–13.

Lavender, A., Nu, F. & Symes, W.W., 2005. Imaging teleseismic P to S scattered waves using the Kirchhoff integral, in *Seismic Earth, Array Analysis of Broadband Seismogram, Geophysical Monograph Series,* Vol. 157, pp. 149–169, eds Levender, A. & Nolet, G., AGU, Washington, DC.

Lee, C.-T.A., 2006. Geochemical/Petrological Constraints on the Origin of Cratonic Mantle, *Geophys., Mon. Ser., AGU,* **164,** 89–114.

Lee, C.-T.A., Luffi, P. & Chin, E.J., 2011. Building and destroying continental mantle, *Annu. Rev. Earth planet. Sci.,* **39,** 59–90.

Ludwig, W.J., Nafe, J.E. & Drake, C.L., 1970. Seismic refraction, in *The Sea,* Vol. 4, pp. 53–84, ed. Maxwell, A.E., Wiley-Interscience, New York.

Mitra, S., Pristley, K., Gaur, V.K. & Rai, S.S., 2006. Shear wave velocity structure of the south Indian lithosphere from Rayleigh wave phase velocity measurements, *Bull. seism. Soc. Am.,* **96,** 1551–1559.

Naqvi, S.M. & Rogers, J.J.W., 1987. *Precambrian Geology of India,* Oxford University Press, 223 pp.

Oreshin, S.I., Vinnik, L.P., Kiselev, S.G., Rai, S.S., Prakasam, K.S. & Treussov, A.V., 2011. Deep seismic structure of the Indian shield, western Himalaya, Ladakh and Tibet, *Earth planet. Sci. Lett.,* **307,** 415–429.

Prakasam, K.S. & Rai, S.S., 1998. Teleseismic delay-time tomography of the upper mantle beneath southeastern India: imprint of Indo-Antarctica rifting, *Geophys. J. Int.,* **133,** 20–30.

Priestley, K., 1999. Velocity structure of the continental upper mantle: evidence from southern Africa, *Lithos,* **48,** 45–56.

Priestley, K. & Debayle, E., 2003. Seismic evidence for a moderately thick lithosphere beneath the Siberian Platform, *Geophys. Res. Lett.,* **30,** doi:10.1029/2002GL015931.

Priestley, K. & McKenzie, D., 2006. The thermal structure of the lithosphere from shear wave velocities, *Earth planet. Sci. Lett.,* **244,** 285–310.

Priestley, K. & McKenzie, D., 2013. The relationship between shear wave velocity, temperature, attenuation and viscosity in the shallow part of the mantle, *Earth planet. Sci. Lett.,* **381,** 78–91.

Radhakrishna, B.P., 1983. Archean granite-greenstone terrain of the south Indian shield, in *Precambrian of south India*, *Mem. Geol. Soc. India,* **4,** 1–46.

Rai, S.S., Borah, K., Das, Ritima, Gupta, S., Shalivahan, Prakasam, K.S., Sivaram, K., Sudesh, Kumar & Meena, R., 2013. The South India

Precambrian crust and shallow lithospheric mantle: initial results from the India Deep Earth Imaging Experiment (INDEX), *J. Earth Syst. Sci.,* **122,** 1435–1453.

Ramesh, D.S., Bianchi, M.B. & Das Sharma, S., 2010. Images of possible fossil collision structures beneath the Eastern Ghats belt, India, from P and S receiver functions, *Lithosphere,* **2,** 84–92.

Roy Chowdhury, K. & Hargraves, R.B., 1981. Deep seismic soundings in India and the origin of the continental crust, *Nature,* **291**(5817), 648–650.

Roy, S. & Mareschal, J.-C., 2011. Constraints on the deep thermal structure of the Dharwar craton, India, from heat flow, shear wave velocities, and mantle xenoliths, *J. geophys. Res.,* **116,** B02409, doi:10.1029/2010JB007796.

Schutt, D.L. & Lesher, C.E., 2006. Effects of melt depletion on the density and seismic velocity of garnet and spinel lherzolite, *J. geophys. Res.,* **111,** B05401, doi:10.1029/02003JB002950.

Shapiro, N.M. & Ritzwoller, M.H., 2002. Monte-Carlo inversion for a global shear velocity model of the crust and upper mantle, *Geophys. J. Int.,* **151,** 88–105.

Srinagesh, D. & Rai, S.S., 1996. Teleseismic tomographic evidence for contrasting upper mantles in south Indian Archean terrains, *Phys. Earth planet. Int.,* **97,** 27–41.